PHYSICAL REVIEW C VOLUME 26, NUMBER 1 JULY 1982

# Analyzing power of proton-nucleus elastic scattering between 80 and 180 MeV

P. Schwandt, H. O. Meyer, W. W. Jacobs, A. D. Bacher, S. E. Vigdor,
and M.D. Kaitchuck
*Indiana University Cyclotron Facility, Bloomington, Indiana 47405*

T. R. Donoghue
*Ohio State University, Columbus, Ohio 43212*

(Received 25 January 1982)

Elastic scattering of polarized protons of 80—180 MeV from a number of target nuclei $(24 < A < 208)$ has been measured. The systematic energy and target mass dependence of the cross section and analyzing power angular distributions is discussed. The data have been analyzed within the framework of a conventional optical potential model, and the behavior of the potential parameters as a function of energy is investigated. Comparisons are made with results obtained at energies greater than 180 MeV and with predictions obtained from microscopic models.

NUCLEAR REACTIONS $^{24}\mathrm{Mg}(\vec{p},p)$, $E_p=134.7$ MeV; $^{28}\mathrm{Si}(\vec{p},p)$, $E_p=134.5$ MeV; $^{40}\mathrm{Ca}(\vec{p},p)$, $E_p=80.2$, 181.5 MeV; $^{90}\mathrm{Zr}(\vec{p},p)$, $E_p=79.6$, 98.7, 134.8, 160 MeV; $^{92}\mathrm{Zr}(\vec{p},p)$, $E_p=104$ MeV; $^{120}\mathrm{Sn}(\vec{p},p)$, $E_p=104$ MeV; $^{208}\mathrm{Pb}(\vec{p},p)$, $E_p=79.8$, 98, 182 MeV; measured $\sigma(\theta)$, $A_y(\theta)$; optical-model analysis, deduced energy dependence, comparison with microscopic models.

## I. INTRODUCTION

For proton-nucleus scattering, the importance of the projectile spin dependent interaction increases dramatically relative to the central part as one increases the bombarding energy to the medium-energy range. For example, a recent investigation focusing on cross-section $\sigma(\theta)$ measurements[1] showed a surprising sensitivity of $\sigma(\theta)$ to the spin-orbit potential, manifested in a pronounced damping of the characteristic diffractive oscillations at intermediate angles for bombarding energies greater than ~100 MeV. Although the spin-orbit potential parameters were better defined by the cross-section measurements than expected, appreciable ambiguities and uncertainties remained. More and higher-quality polarization data were called for in order to refine the parametrization of the spin-dependent potential in this energy regime.

This paper reports the results of an experimental program in proton-nucleus elastic scattering between 80 and 180 MeV carried out with a polarized proton beam at the Indiana University Cyclotron Facility. The data presented here are restricted to analyzing power measurements since most of the corresponding cross section angular distributions have already been reported in the literature. Details of the experimental procedure and a list of the data incorporated in the analysis are given in Sec. II. In Sec. III we discuss the physics implications of the present measurements. On the one hand, the survey nature of this program lends itself to a search for simple, predominant characteristics of proton elastic scattering analyzing powers $A_y(\theta)$ as a function of bombarding energy and target mass. On the other hand, we want to deduce the systematic behavior of the relevant parameters in a phenomenological optical model description of the scattering. A comparison of these results with other optical model studies and with the predictions of microscopic models completes Sec. III. A brief summary of our conclusions is given in Sec. IV.

The optical-model analysis presented here is conventional in the sense that the radial dependence of the optical potentials is of the Woods-Saxon (or Woods-Saxon derivative) type. Recently, evidence has been accumulating[2] that such a simple parametrization may not be adequate beyond a bombarding energy of about 150 MeV. In the present work, this aspect of the optical model is discussed only briefly; a detailed investigation of the implications of nonstandard potential shapes for intermediate-energy proton scattering will be the subject of a forthcoming communication. Preliminary accounts of parts of the present analysis have been reported previously.[1,3]

## II. EXPERIMENT

### A. General apparatus

The polarized proton beam used to carry out our measurements was supplied by the Indiana University Cyclotron Facility (IUCF). The targets bombarded ranged in thickness from a few to about 50 mg/cm$^2$. The Si (92% $^{28}$Si) and Ca (97% $^{40}$Ca) targets were of natural isotopic composition; in the cases of $^{24}$Mg, $^{90,92}$Zr, $^{120}$Sn, and $^{208}$Pb, isotopically enriched elements ($>95\%$ enrichment) were used. The uncertainty of the bombarding energy was always less than $\sim 150$ keV. The total beam charge was determined by integrating the beam current in a Faraday cup embedded in concrete shielding. For scattering angles less than 20°–24°, the primary beam would intercept the yoke of the spectrometer magnet, thus a small Faraday cup mounted on a movable table inside the scattering chamber was used. After proper alignment of the cup with the beam, separate charge collection from the left and right halves of the cup provided a difference signal for automatic centering of the beam.

The scattered protons were detected using a magnetic spectrometer.[4] The overall energy resolution was sufficient in all cases to resolve the major contaminant contributions (due to $^{12}$C and $^{16}$O) in the energy spectra from the elastic proton group of interest; this proton group, however, included contributions from all isotopes present for a given target element. The positioning in angle of the spectrometer is known to better than $\pm 0.05°$. The origin of the angle scale was determined from measurements on both sides of the beam. The angular acceptance of the spectrometer in the scattering plane varied, but was always kept smaller than $\Delta\theta_{\mathrm{lab}} = \pm 0.55°$. The detector arrangement in the focal plane included a helical wire proportional chamber for position information, followed by two plastic $\Delta E$ scintillators for particle identification. The dead time of the data acquisition system was measured by processing pulser events, generated at a (known) rate proportional to the instantaneous beam current, in a manner similar to that employed for the real events.

### B. Polarized beam

The polarized hydrogen beams at IUCF are produced by a commercially available atomic-beam polarized ion source[5] located in one of the high-voltage preinjector terminals. The source output is typically 10–20 $\mu$A of about 70% polarized protons. The orientation of the spin alignment axis is chosen by selecting one of two atomic-beam hyperfine-transition radio-frequency cavities located in regions of weak or strong magnetic field, respectively. Thus the spin orientation can be changed rapidly without affecting beam transmission or intensity. Switching between spin orientations is done remotely under computer control.

The polarization of the beam is measured after acceleration in the first-stage (injector) cyclotron at proton energies of 9–13 MeV by inserting a polarimeter into the beam. The polarimeter unit consists of a pair of entrance slits with current measurement for automatic centering of the beam, a gas cell containing $^4$He at a pressure of $2\times10^5$ Pa and a Faraday cup as beam stop. The gas cell is a cylinder of 3.8 cm diameter with Havar[6] walls of 6 $\mu$m thickness. Protons elastically scattered from $^4$He are observed symmetrically at $\theta_{\mathrm{lab}} = \pm 112°$ using 500 $\mu$m thick silicon surface barrier detectors. From the left-right asymmetry and the known $^4\mathrm{He}(\vec{p},p)^4\mathrm{He}$ analyzing power[7] the beam polarization $P$ is deduced. Assuming that during the subsequent acceleration in the main-stage cyclotron the polarization of the beam is not significantly reduced, the above procedure constitutes a measurement of the beam polarization on target. To verify this assumption we compared analyzing power measurements for $^{12}\mathrm{C}(\vec{p},p)^{12}\mathrm{C}$ made at IUCF, using the above method for determining $P$, with published elastic $p + {}^{12}\mathrm{C}$ polarization data[8] which had been obtained in (or normalized to) double-scattering experiments. The results of these tests, which were conducted at a number of bombarding energies between 120–185 MeV, are shown in Fig. 1. From the agreement (within statistical errors) between the data obtained by the two methods, it can be concluded that the uncertainty in the absolute normalization of the polarization for the beam on target, and thus of the analyzing powers measured by this technique, is less than $\pm 0.02$.

### C. Procedure

For each target and each angle setting of the spectrometer, runs of about equal integrated beam current were taken with the polarization vector of the incident protons up or down with respect to the scattering plane. Periodically, the beam polarization was determined in the manner described in Sec. II B. From the beam polarizations for spin up and

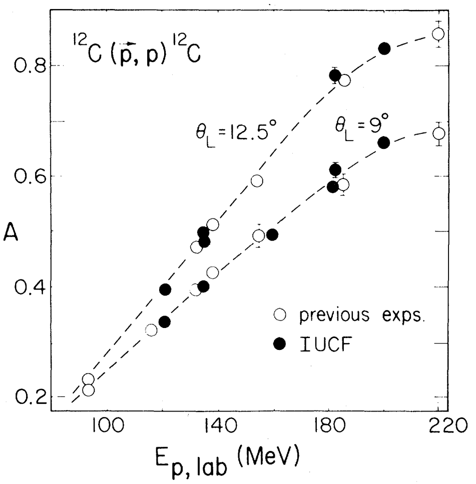

FIG. 1. Analyzing powers for proton elastic scattering from $^{12}$C at laboratory angles of 9° and 12.5° and bombarding energies between 90 and 220 MeV. Open circles are previous data from various sources (Ref. 8), solid symbols are results of measurements with the IUCF polarized proton beam, assuming beam polarizations given by the low-energy $^{4}$He polarimeter as described in Sec. II B. The dashed curves are meant only to guide the eye.

down, the integrated beam current, the measured dead time, the known target thickness, and the acceptance solid angle of the spectrograph, $\sigma(\theta)$ and $A_y(\theta)$ were calculated in the usual manner. In angular regions where the measurements showed strong curvature, the raw data of $\sigma(\theta)$ and $\sigma(\theta)A_y(\theta)$ were corrected for the nonlinear variation of the observables across the angular acceptance $\Delta\theta$ of the spectrometer by locally fitting these quantities with second-order polynomials in $\theta$ to determine, e.g., the derivative $\sigma'' \equiv d^2\sigma/d\sigma^2$ required to compute $\sigma_{\text{corr}} \simeq \sigma + \sigma''(\delta\theta)^2/3$, where $\delta\theta = \Delta\theta/3$ (and similarly for $\sigma A_y$). These corrections were seldom larger than the statistical uncertainties in the measurements. At angles smaller than 20°–24° an additional normalization correction was necessary because the beam charge was not completely collected by the small internal Faraday cup as a result of outscattering and incomplete electron suppression.

The total experimental errors assigned to the $A_y$ data include, besides the statistical contribution (ranging from $\pm 0.005$ to $\pm 0.025$), the uncertainties associated with dead time correction and with charge integration (each contributing up to $\pm 0.005$), a possible change in the beam polarization during a run (typically $\Delta P < 0.01$) and an uncertainty of the actual scattering angle of $\pm 0.05°$. These errors were combined in quadrature to form the total relative error in $A_y(\theta)$ which ranged from $\pm 0.015$ to $\pm 0.04$, typically. Not included are error contributions from possible, small left-right shifts of the beam spot on target between runs, and from target nonuniformity. These could lead to a significant error when detecting protons only on one side of the beam, as was done here. However, the reproducibility of the measurements was checked repeatedly (generally yielding agreement to within 0.02 or better), and in the later stages of the experiment (i.e., measurements at 80 MeV) the provision for "fast" reversal of the spin alignment axis was introduced, making analyzing power measurements insensitive to any slow change of the beam characteristics on target. The switching of the spin orientation (typically every 60 s) and the corresponding routing of the accumulated data were done automatically by computer control.

The overall scale (or normalization) error in the $A_y$ measurements, arising principally from the uncertainty of the absolute value for the beam polarization and from other systematic effects (thought to be of order 0.01), is estimated to be at most 3%.

### D. Data

The data presented in this paper include analyzing power measurements $A_y(\theta)$ made at IUCF for 80–180 MeV protons elastically scattered from a number of targets, ranging from $^{24}$Mg to $^{208}$Pb. In some cases, for completeness, comparison is made with angular distributions of $A_y(\theta)$ obtained at other institutions.[9–11] These data are illustrated in Figs. 2–4. The relative uncertainties in the $A_y$ data are generally smaller than the size of the points, or are indicated by error bars where they exceed the dot size. A complete list of targets and proton energies covered in this investigation, together with the corresponding number and range of scattering angles, is given in Table I. Also listed in Table I is similar information regarding the cross section measurements used in the present optical model analysis. Although the present experiment yielded cross section data as well as analyzing powers, the cross section angular distributions used in our analysis were taken from a more complete earlier experiment at IUCF using an unpolarized beam.[1] In one case, $\sigma(\theta)$ data obtained at Maryland[12] were adopted. The beam energies quoted in Table I are known to within $\pm 150$ keV if a figure after the decimal point is given. In all other cases, the bombarding energy is not known to better than 0.5 MeV.

The results for elastic scattering from the nuclei

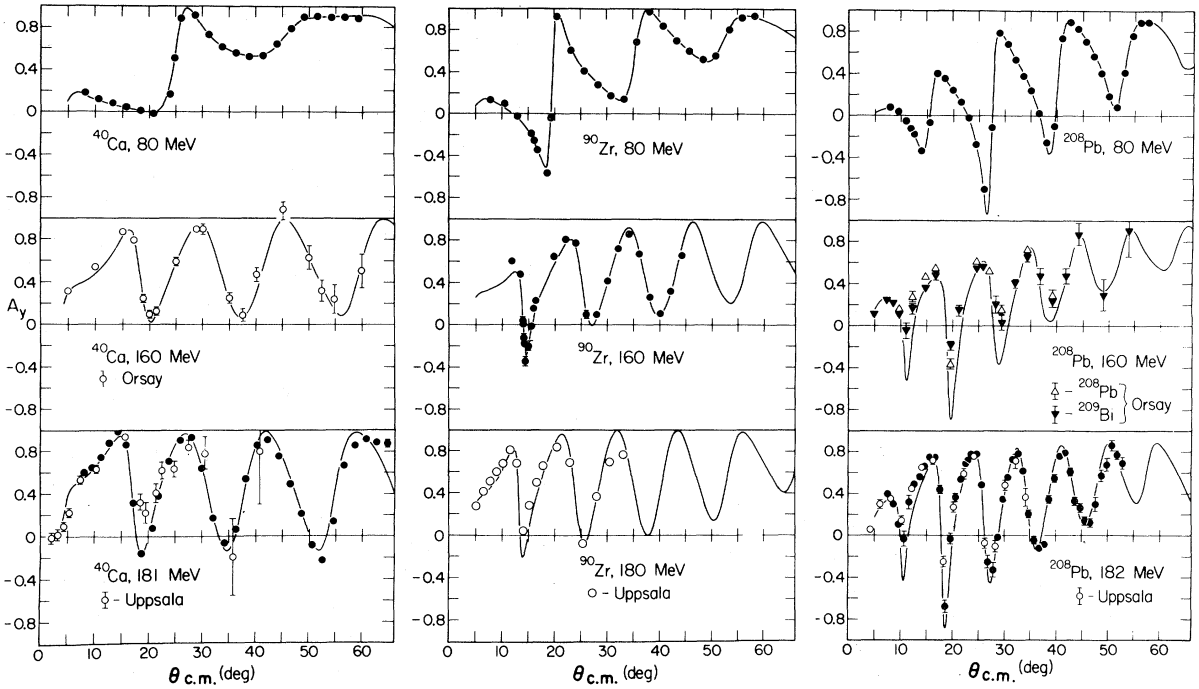

FIG. 2. Analyzing powers $A_y$ for 80, 160, and ~180 MeV protons elastically scattered from $^{40}$Ca (left panel), $^{90}$Zr (middle panel), and $^{208}$Pb (right panel). Solid circles are IUCF measurements, open symbols (and all triangles) are from other sources as indicated (Orsay: Refs. 9 and 10; Uppsala: Ref. 11). The curves are results of simultaneous optical-model fits to the $A_y$ data and associated $\sigma$ data (cf. Table I).

$^{24}$Mg, $^{28}$Si, $^{92}$Zr, and $^{120}$Sn were obtained as the byproduct of inelastic proton scattering measurements, not specifically aimed at observing the ground state transition. These IUCF experiments were mainly concerned with exploring the giant resonance region[13] and with investigating the excitation of high spin states.[14]

## III. ANALYSIS

### A. Characteristic features of the analyzing powers and their interpretation

The analyzing powers presented in Figs. 2—4 exhibit some simple systematic features as a function of proton energy and target mass. For light and medium-mass targets, $A_y(\theta)$ is predominantly positive, maintaining large values ($A_y > 0.5$) beyond $\theta = 30°$ at lower energies ($T_p < 100$ MeV), but oscillating in a regular manner between approximately $A_y = 0$ and $A_y = +1$ at the higher energies ($T_p > 150$ MeV). For heavy targets (e.g., $^{208}$Pb) the oscillations are more pronounced, with sizable negative excursions. As pointed out in Refs. 1 and 3, these features, when viewed in a larger context [i.e., over a wider energy range and in combination with the characteristic features of the differential cross section $\sigma(\theta)$], can be understood in terms of "spin-channel dominance": At both low and high energies ($T_p < 100$ MeV and $T_p > 300$ MeV), the partial cross sections $\sigma^+(\theta)$ and $\sigma^-(\theta)$ corresponding to $\langle \vec{\sigma} \cdot \hat{n} \rangle = \pm 1$ (incident proton spin up or down with respect to the scattering plane) are ordered in magnitude as $\sigma^+ \gg \sigma^-$ beyond some moderately forward angle. Consequently, the angular structure of $\sigma(\theta) \equiv \sigma^+ + \sigma^-$ is dominated by the oscillatory $\sigma^+$, and $A(\theta) \equiv (\sigma^+ - \sigma^-)/(\sigma^+ + \sigma^-)$ approaches unity. In the "transition energy" region of 150—250 MeV, on the other hand, $\sigma^+$ and $\sigma^-$ in the forward hemisphere are found to oscillate with comparable amplitudes but with slightly different angular periods; hence, $\sigma^+$ and $\sigma^-$ move out of phase over a portion of the angular range, leading to an angular distribution for $\sigma(\theta)$ with little structure and strong oscillations in $A_y(\theta)$.

In a potential model, the relative phasing of $\sigma^+$ and $\sigma^-$ is sensitive to the interplay of the complex central potential $U_c$ and the complex spin-orbit po-

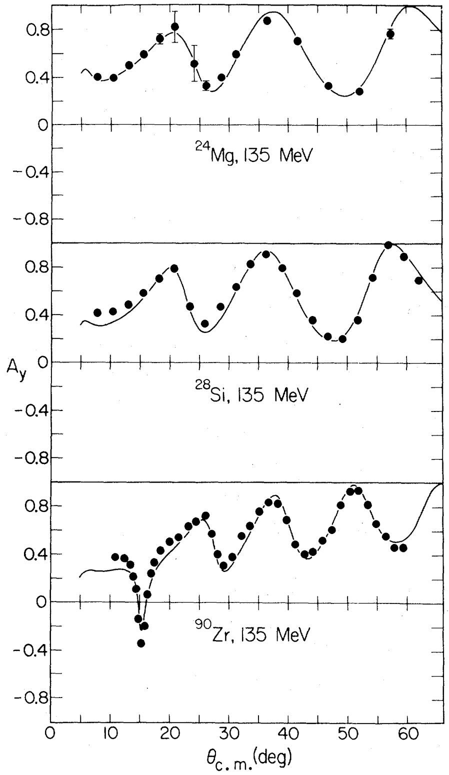

FIG. 3. Analyzing powers for 135 MeV protons elastically scattered from $^{24}$Mg, $^{28}$Si, and $^{90}$Zr (all IUCF data). The curves are results of simultaneous optical-model fits to the $A_y$ data and associated $\sigma$ data (cf. Table I).

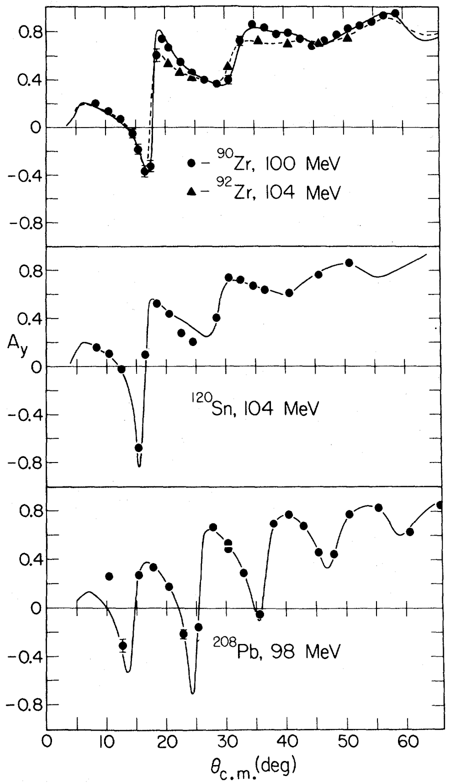

FIG. 4. Analyzing powers for protons elastically scattered from $^{90,92}$Zr, $^{120}$Sn, and $^{208}$Pb near 100 MeV bombarding energy (all IUCF data). The curves are results of simultaneous optical-model fits to the $A_y$ data and associated $\sigma$ data (cf. Table I).

TABLE I. List of analyzing power data (subscript $A$) and differential cross section data (subscript $\sigma$) used in the present optical model analysis (Sec. III). Given are the number of data points ($N$), the c.m. angular range ($\theta$) covered, and the source of the data (Ref).

| Target | $T_p$ (MeV) | $N_A$ | $\theta_A$ | Ref. | $N_\sigma$ | $\theta_\sigma$ | Ref. |
|---|---|---|---|---|---|---|---|
| $^{24}$Mg | 134.7 | 17 | 7.9°–57.2° | present work | 17 | 7.9°–57.2° | present work |
| $^{28}$Si | 134.5 | 22 | 7.8°–62.0° | present work | 42 | 6.7°–88.5° | 1 |
| $^{40}$Ca | 80.2 | 22 | 8.1°–59.2° | present work | 45 | 5.3°–94.7° | 1 |
| | 153 | 18 | 5.2°–61.2° | 9,10 | 43 | 7.9°–87.9° | 1 |
| | 181.5 | 31 | 7.9°–68.8° | present work | 33 | 7.9°–68.8° | present work |
| $^{90}$Zr | 79.6 | 24 | 7.9°–58.4° | present work | 60 | 6.3°–90.9° | 1 |
| | 98.7 | 29 | 8.3°–58.9° | present work | 39 | 15.5°–76.8° | 12 |
| | 134.8 | 40 | 10.9°–59.4° | present work | 99 | 6.1°–126.1° | 1 |
| | 160 | 27 | 11.9°–44.2° | present work | 52 | 4.7°–81.9° | 1 |
| | 185 | 17 | 5.1°–32.8° | 11 | 45 | 6.4°–86.1° | 1 |
| $^{92}$Zr | 104 | 14 | 12.5°–50.8° | present work | 14 | 12.5°–50.8° | present work |
| $^{120}$Sn | 104 | 17 | 8.4°–50.7° | present work | 17 | 8.4°–50.7° | present work |
| $^{208}$Pb | 79.6 | 35 | 7.8°–57.6° | present work | 59 | 6.2°–93.5° | 1 |
| | 98 | 23 | 10.3°–75.5° | present work | 23 | 10.3°–75.5° | present work |
| | 153 | 11 | 7.5°–40.2° | 9,10 | 72 | 6.1°–77.4° | 1 |
| | 182.0 | 47 | 7.6°–52.8° | present work | 51 | 6.3°–80.1° | 1 |

tential $U_{\mathrm{SO}}$. Since the strength of $U_{\mathrm{SO}}$ is proportional to the incident momentum, it becomes increasingly more important relative to $U_c$ with increasing energy until $\sim 300$ MeV, where the scattering becomes dominated by the rapidly growing absorptive (imaginary) part of the central potential. The *mechanisms* for $\sigma^+$ dominance at higher and at lower energies (above and below the transition energy region) are thus very different: (1) at *higher* energies, one finds $\sigma^+ > \sigma^-$ because of the strong difference in absorption for opposite signs of $\vec{\sigma}\cdot\vec{l}$ for protons incident on the essentially black-sphere nucleus,[15] while (2) at *lower* energies the scattering is dominated by the surface partial waves, for which the predominantly real nuclear potential is more attractive in the $\langle \vec{\sigma}\cdot\hat{n} \rangle = +1$ spin state. Hence, in the latter case, the semiclassical deflection angles $\Theta$ for surface impact obey $\Theta^+ > \Theta^-$, i.e., at a given impact parameter, spin-up incident protons scatter through a larger angle than their spin-down counterparts. Consequently, $\sigma^+(\theta) > \sigma^-(\theta)$ because of the systematic decrease of $\sigma(\theta)$ with increasing $\theta$. This behavior is reminiscent of the semiclassical rainbow scattering mechanism describing medium-energy deuteron scattering[16]; in fact, the rainbow scattering of protons [i.e., enhancement of $\sigma(\theta)$ around $\theta = \Theta_{\max}$ followed by exponential falloff in the classically forbidden region $\theta > \Theta_{\max}$, coupled with $A_y \approx +1$], observed here only in subdued form because of absorption, can be brought out clearly in a model calculation by reducing the strength of the imaginary central potential.

### B. Optical model analysis

The local optical potential used in the analysis of the data listed in Table I was parametrized as

$$U(r) = U_{\mathrm{Coul}}(r) - Vf_0(r) - iWf_w(r) + \frac{2.00}{r}\left[ V_{\mathrm{SO}}\frac{d}{dr}f_{v\mathrm{SO}}(r) + iW_{\mathrm{SO}}\frac{d}{dr}f_{w\mathrm{SO}}(r) \right] \vec{\mathrm{L}}\cdot\vec{\sigma} \ , \quad (1)$$

with Woods-Saxon form factors $f_x(r;r_x,a_x)$. Using the code[17] SNOOPY8, the potential parameters were adjusted for each case to fit simultaneously the angular distribution of the cross section, $\sigma(\theta)$, and the analyzing power, $A_y(\theta)$. Relativistic effects were treated in an approximate way as described in Ref. 1. The starting parameters were taken from the "fixed-spin-orbit" fits to the cross section data by Nadasen *et al.*[1]

Initially, all 12 parameters of the four nuclear potential terms (central and spin-orbit, real and imaginary parts) were varied in unconstrained "best-fit" searches on the data. Angular distributions of $A_y(\theta)$ calculated from these best-fit parameters are compared with the data in Figs. 2–4. The corresponding fits to the differential cross sections do not differ noticeably from those in Ref. 1 and for that reason are not reproduced here. The quality of fits to the $A_y(\theta)$ data is satisfactory overall, and excellent for most of the IUCF measurements.

Several of the geometry parameters obtained in the unconstrained fits exhibited smooth, essentially linear variations with proton energy $T_p$. In particular, most of the geometry parameters of the complex spin-orbit (SO) potential exhibited little or no dependence on $T_p$. Hence, in order to reduce the scatter of individual parameter values with $T_p$, we proceeded to constrain successively more of the SO potential geometry to energy-independent values until finally all four parameters $r_{v\mathrm{SO}}$, $a_{v\mathrm{SO}}$, $r_{w\mathrm{SO}}$, and $a_{w\mathrm{SO}}$ were held fixed in the parameter searches without deterioration in the overall quality of fit. Over the energy range $80 \le T_p \le 180$ MeV and target mass range $40 \le A \le 208$, these SO geometry parameters are well represented by the analytic relations (with $T_p$ in MeV, $r$ and $a$ in fm)

$$\begin{aligned} r_{v\mathrm{SO}} &= 0.920 + 0.0305A^{1/3} \ , \\ a_{v\mathrm{SO}} &= \begin{cases} 0.768 - 0.0012T_p, & T_p \le 140 \text{ MeV} \\ 0.60, & T_p > 140 \text{ MeV} \end{cases} \\ r_{w\mathrm{SO}} &= 0.877 + 0.0360A^{1/3} \ , \\ a_{w\mathrm{SO}} &= 0.62 \ . \end{aligned} \quad (2)$$

The only notable deviation from these relations is found for $^{24}$Mg and $^{28}$Si at 135 MeV where $r_{v\mathrm{SO}}$ and $r_{w\mathrm{SO}}$ are somewhat smaller (0.98 and 0.96 fm, respectively).

While constraining the geometry of the spin-orbit potential, we adjusted the remaining parameters to fit the data. The resulting values are presented as a function of the energy in Fig. 5 (solid symbols). The trend of most parameters with energy is readily apparent: Central potential geometry parameters vary linearly with $T_p$ and show no systematic dependence on target mass number $A$ (with the possible exception of $r_0$ at the higher energies); the strengths $V, V_{\mathrm{SO}}$ of the real central and SO potentials decrease linearly with increasing $\ln T_p$ and exhibit a noticeable dependence on $A$ [consistent with $(N-Z)/A$ asymmetry]; the imaginary central strength $W$ increases rapidly with $T_p$ at the higher

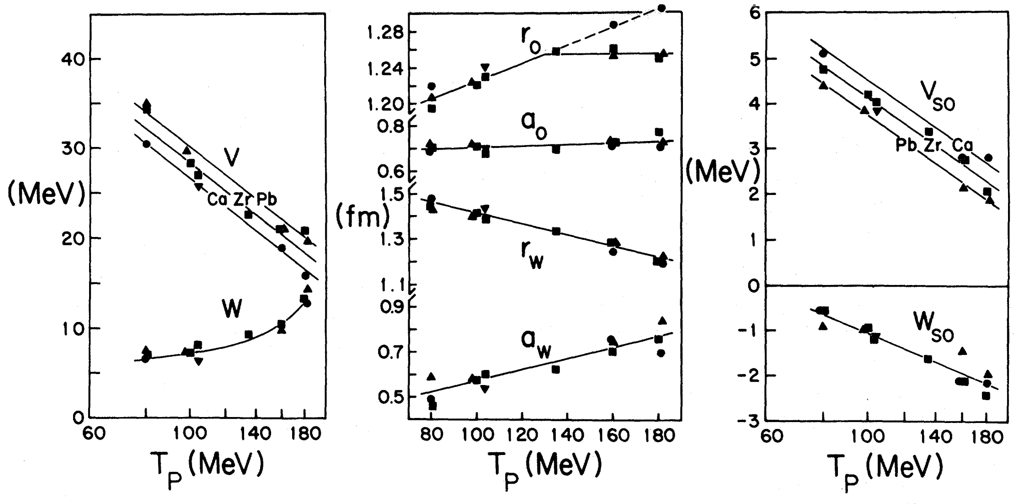

FIG. 5. Energy dependence of the optical model parameters obtained in the present analyses of $^{40}$Ca (circles), $^{90,92}$Zr (squares), and $^{208}$Pb (triangles) for the fixed spin-orbit geometry of Eq. (2). The lines represent the average trend of the results described by Eq. (3). Note the logarithmic proton energy scale for the central potential strengths (left panel) and the spin-orbit potential strengths (right panel).

energies, and the magnitude of the imaginary SO strength $W_{SO}$ increases strongly with increasing $\ln T_p$, becoming comparable to the real SO strength $V_{SO}$ near 200 MeV; neither $W$ nor $W_{SO}$ show any systematic $A$ dependence. The straight lines and curves in Fig. 5 represent least-squares fits to the potential parameters which resulted in the following functional dependences on $T_p$ (in MeV) and $A$ over the ranges $80 \le T_p \le 180$ MeV, $40 \le A \le 208$ (with $V$ and $W$ in MeV, $r$ and $a$ in fm):

$$V = 105.5(1-0.1625\ln T_p)+16.5(N-Z)/A \; ,$$

$$r_0 = \begin{cases} 1.125+1.0\times 10^{-3}T_p \; , & T_p \le 130\,\text{MeV} \\ & (T_p \le 180\,\text{MeV for Ca}) \\ 1.255, & T_p > 130\,\text{MeV} \\ & (\text{except for Ca}) \end{cases}$$

$$a_0 = 0.675+3.1\times 10^{-4}T_p \; , \qquad (3)$$

$$W = 6.6+2.73\times 10^{-2}(T_p-80) + 3.87\times 10^{-6}(T_p-80)^3 \; ,$$

$$r_w = 1.65-2.4\times 10^{-3}T_p \; ,$$

$$a_w = 0.32+2.5\times 10^{-3}T_p \; ,$$

$$V_{SO} = 19.0(1-0.166\ln T_p)-3.75(N-Z)/A \; ,$$

$$W_{SO} = 7.5(1-0.248\ln T_p) \; .$$

[Note that $W_{SO} < 0$ over the whole energy range. $W_{SO}$ represents the spin-dependent *modification* of the central imaginary potential in the surface region; hence, a negative value obtained for $W_{so}$ does *not* imply flux creation.]

The specific functional relations chosen to represent the $T_p$ and $A$ dependences of the potential parameters are phenomenological, i.e., not guided by any physical model. These $T_p$ and $A$ dependences determined in the present analysis of an extensive set of $\sigma(\theta)$ and $A_y(\theta)$ data differ *quantitatively* from those found in the earlier analysis of predominantly $\sigma(\theta)$ data by Nadasen *et al.*[1] [which included only a few $A_y(\theta)$ measurements]. However, the *qualitative* behavior of the parameters with energy is fairly similar in the two analyses. The results of the present analysis thus largely substantiate the Nadasen results for the medium-energy proton optical potential within the specific framework of the conventional Woods-Saxon parametrization. In particular, we confirm the preliminary conclusions of Nadasen *et al.*[1] concerning the energy systematics of the proton SO potential, and the need for a sizable imaginary SO component. Worthy of note are the relative energy and isospin dependences of the real SO and real central potentials: One finds $(1/V_{SO})\delta V_{SO}/\delta T_p = (1/V)\,\delta V/\delta T_p$ (in disagreement with a naive expectation[18] based on the different nonlocality ranges for the two potential terms), and an $(N-Z)$ dependence of $V_{SO}$ of opposite sign to that of $V$ (in agreement with schematic model expectations[19]).

### C. Comparison with other optical potential studies

The question of the uniqueness of phenomenological analyses of elastic scattering data when one uses a specific analytic radial shape for the potential (e.g., the Woods-Saxon or Fermi-function shape) has been addressed in Refs. 1 and 2. Recent phenomenological analyses[20] of 120–200 MeV $\vec{p}+{}^{12}C$ data, extending over a considerably larger range of momentum transfer than most medium-energy data (including the present data), as well as a global analysis of $\vec{p}+{}^{40}Ca$ data over the energy range $30 < T_p < 1000$ MeV in a relativistic Dirac-Hartree model,[21] have demonstrated that *real central potential* shapes deviating radically from the monotonic Woods-Saxon (WS) form are consistent with, if not necessary to explain, the measurements for proton energies beyond $\sim 150$ MeV. Indeed, microscopic-model calculations[22,23] suggest that at such energies the proton-nucleus real central potential should have a pronounced depression just inside the nuclear surface. The strong energy dependence of some of the WS geometry parameters found in the present analysis is likely to be caused (at least partly) by the unphysical constraint imposed on the analysis by the use of WS form factors. The present parametrization is obviously adequate for providing a very good description of existing $\sigma(\theta)$ and $A_y(\theta)$ data up to 180 MeV, as illustrated by the quality of the present fits. However, the prospective user of the present results (who may wish to generate distorted proton waves for reaction calculations) should be aware that the potential derived here may be only phase-shift equivalent to more physical, non-WS potentials which also describe the elastic data, but may yield significantly different proton wave functions inside the nuclear surface.

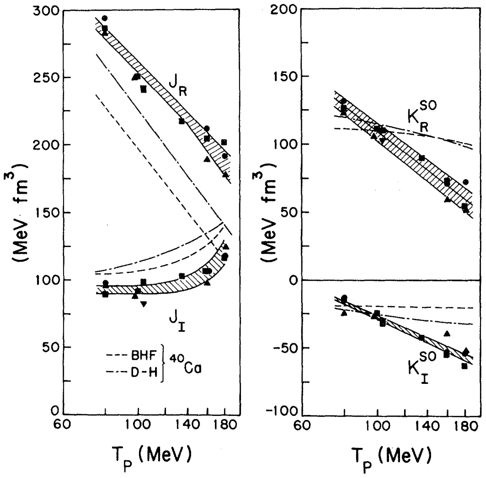

FIG. 6. Energy dependence of the volume integrals of the complex central potential (left panel) and the complex spin-orbit potential (right panel) defined in the text (Sec. III C). Symbols denote the individual results for $^{40}$Ca (circles), $^{90,92}$Zr (squares), and $^{208}$Pb (triangles). Shaded bands represent the variation of these quantities with $T_p$ and target mass given by the average parametrization of the potentials [Eqs. (2) and (3)]. Dashed curves are predictions of microscopically-based potential models (BHF: Ref. 22; D-H: Ref. 21).

In discussions of global optical model fits, it has been customary to describe the systematic behavior of the phenomenological optical potential in terms of volume integrals and rms radii of the potentials, since these properties appeared to be better determined than individual potential parameters. In order to make contact with previous phenomenological analyses which have also employed WS form factors, we shall follow this procedure here. However, we warn against attaching too much physical significance to the volume integrals, since they are undoubtedly sensitive to the form assumed for the radial dependence of the potential.

Volume integrals of the complex central potential (WS form) and of the complex SO potential (Thomas form) determined in the present analysis are presented as functions of bombarding energy $T_p$ in Fig. 6 (solid symbols) for the constrained SO geometry case. In terms of the radial integrals

$$I_k \equiv 4\pi \int U_k(r) r^2 dr$$

for each of the four nuclear potential terms ($k=0,w,v\mathrm{SO},w\mathrm{SO}$), the quantities shown are defined as $J_R \equiv I_0/A$, $J_I \equiv I_w/A$, $K_R \equiv I_{v\mathrm{SO}}/A^{1/3}$, and $K_I \equiv I_{w\mathrm{SO}}/A^{1/3}$. The shaded bands in Fig. 6 represent the values calculated from the analytical expressions for the potential parameters. Although fluctuations of order 5–10% around an average value are observed in the empirical volume integrals, little or no systematic dependence on target mass is observed for the central components $J_R$ and $J_I$. This is in agreement with empirical results at lower energies[24] and with theoretical expectations.[25] For the real SO potential, the $(N-Z)$ asymmetry of the strength $V_{\mathrm{SO}}$ is only partly canceled by the $A$ dependence of the radius parameter $r_{\mathrm{SO}}$, resulting in the residual target dependence seen in the volume integral $K_R = 8\pi V_{\mathrm{SO}} r_{\mathrm{SO}}$. The energy dependence of all four volume integrals essentially reflects the energy dependence of the corresponding strength parameters.

The dashed and dotted-dashed curves in Fig. 6 are microscopic predictions of the local optical potential based on a Brueckner-Hartree-Fock nuclear matter approach[22] (dashed curves), and results of the phenomenological Dirac-Hartree model[21] based on relativistic mean field theory (dotted-dashed curves). For the real central potential, the form factors of these microscopic potentials are quite different from the WS form chosen for the phenomenological parametrization, which accounts for the discrepancy between empirical and theoretical values for $J_R$. On the other hand, for the imaginary central and the complex SO potentials, the form factors of the phenomenological and microscopic models are sufficiently similar at all energies to make comparison of their volume integrals $J_I$, $K_R$, and $K_I$ meaningful. However, the apparent similarity of empirical and theoretical $J_I$ values masks some important intrinsic differences between the respective potentials: The microscopic imaginary potential tends to have a larger central strength but slightly shorter range. Also, the energy dependence found for the empirical SO potential volume integrals is stronger than is expected on the basis of the two microscopic models. Since the geometrical shapes of the SO potentials are fairly similar, this observation implies a considerable discrepancy in SO strength for energies beyond $\sim 100$ MeV: The empirical real SO strength falls off too fast with increasing $T_p$, while at the same time the empirical imaginary SO strength increases too rapidly in magnitude. These large differences are a direct consequence of the strong correlation between the surface-peaked SO potential and the assumed radial dependence of the central potential. Model calculations show that any appreciable deviation from the WS form results in significant redistribution of real and imaginary SO strengths in the direction towards the microscopic model predictions. When viewed in this context, *all* volume integrals of the potentials determined in the present analysis are meaningful only in relation to the assumed WS shape for the central potential.

## IV. SUMMARY

Angular distributions of the analyzing power of proton elastic scattering from a number of targets have been measured in the energy range 80–180 MeV. The systematic energy and target mass dependences of the analyzing power (as well as of the associated, previously reported differential cross section) have been discussed in terms of an interplay between the partial cross sections for scattering of protons with spin up or down with respect to the scattering plane.

The inclusion of the new analyzing power data in an optical model analysis using the conventional WS parametrization for the potentials results in quantitative modifications in the set of global potential parameters published earlier,[1] which were based largely on cross section data alone. The absence of qualitative changes can be attributed to the appreciable sensitivity of medium-energy cross sections to the spin-orbit potential.

The present analysis has been carried out in a conventional, local optical model framework (using WS forms for the potentials) in order to relate the results to those of earlier analyses. We feel that this step is necessary before an attempt is made to carry out a global analysis of elastic proton scattering data allowing for substantial departures of the radial potential shape from a WS form, as is expected on the basis of recent experimental work as well as on theoretical grounds.

It has long been believed that volume integrals are more stable against parameter ambiguities and correlations than individual potential parameters, hence volume integrals have been used to compare analyses and study the energy dependence of the local potential. Indeed, volume integrals deduced from the present analysis exhibit a clear systematic dependence on energy and are roughly independent of target mass. On the other hand, the same quantities predicted by two fundamentally different theoretical calculations of the microscopic optical potential are in serious disagreement with the results of the WS phenomenology in regard to their energy dependence. A large part (or all) of this discrepancy in volume integrals is expected to arise from differences in the shapes of the underlying potentials. The notion that potential volume integrals uniquely characterize at least the gross features of the scattering of any particular projectile is thus thrown into doubt by the present comparisons. A further investigation of the consequences of microscopically-based potential shapes would go beyond the scope of the present communication and remains the object of a future study.

---

[1] A. Nadasen, P. Schwandt, P. P. Singh, W. W. Jacobs, A. D. Bacher, P. T. Debevec, M. D. Kaitchuck, and J. T. Meek, Phys. Rev. C 23, 1023 (1981).

[2] H. O. Meyer, P. Schwandt, G. L. Moake, and P. P. Singh, Phys. Rev. C 23, 616 (1981).

[3] P. Schwandt, A. D. Bacher, W. W. Jacobs, H. O. Meyer, and S. E. Vigdor, in *Polarization Phenomena in Nuclear Physics—1980 (Fifth International Symposium,*

*Sante Fe),* Proceedings of the 5th Symposium on Polarization Phenomena in Nuclear Physics, edited by G. G. Ohlsen, R. E. Brown, Nelson Jarmie, M. W. McNaughton, and G. M. Hale (AIP, New York, 1981), p. 457.

[4] R. D. Bent, P. H. Pile, R. E. Pollock, and P. T. Debevec, Nucl. Instrum. Methods 180, 397 (1981).

[5] Auckland Nuclear Accessory Corporation, Auckland, New Zealand (Model 2908C).

[6] Trade name for a cobalt alloy manufactured by Hamilton Technology, Inc., Lancaster, Pennsylvania 17604.

[7] D. C. Dodder, G. M. Hale, N. Jarmie, and K. Witte, Los Alamos Internal Report LA-6389-MS, 1976.

[8] W. G. Chestnut, E. M. Hafner, and A. Roberts, Phys. Rev. 104, 449 (1956); R. Alphonce, A. Johansson, and G. Tibell, Nucl. Phys. 3, 185 (1957); O. N. Jarvis, B. Rose, and J. P. Scanlon, *ibid.* 77, 161 (1966); O. N. Jarvis, *ibid.* 79, 305 (1966); M. R. Wigan, R. A. Bell, P. J. Martin, O. N. Jarvis, and J. P. Scanlon, *ibid.* A114, 377 (1968); A. Ingemarsson, O. Jonsson, and A. Halgren, *ibid.* A319, 377 (1979).

[9] C. Rolland, B. Geoffrion, N. Marty, M. Morlet, B. Tatischeff, and A. Willis, Nucl. Phys. 80, 625 (1966).

[10] A. Willis *et al.,* J. Phys. 30, 13 (1969).

[11] E. Hagberg, A. Ingemarsson, and B. Sundqvist, Phys. Scr. 3, 245 (1971).

[12] K. Kwiatkowski and N. S. Wall, Nucl. Phys. A301, 349 (1978).

[13] S. Kailas, P. P. Singh, A. D. Bacher, D. Friesel, C. C. Foster, P. Schwandt, and J. Wiggins, Indiana University Cyclotron Facility Report P-191, 1982.

[14] S. Yen, R. J. Sobie, T. E. Drake, A. D. Bacher, G. T. Emery, W. P. Jones, D. W. Miller, C. Olmer, P. Schwandt, W. G. Love, and F. Petrovich, Phys. Lett. 105B, 421 (1981).

[15] E. Fermi, Nuovo Cimento II, Suppl. 1, 84 (1955).

[16] E. J. Stephenson, C. C. Foster, P. Schwandt, and D. A. Goldberg, Nucl. Phys. A359, 316 (1981).

[17] P. Schwandt, Indiana University Cyclotron Facility Report No. 81-3, 1981 (unpublished).

[18] M. M. Giannini, J. Phys. G 7, L29 (1981).

[19] J. M. Moss, Phys. Rev. C 17, 813 (1978), and references therein.

[20] P. Schwandt, H. O. Meyer, J. R. Hall, W. W. Jacobs, K. Kwiatkowski, P. P. Singh, and B. C. Clark, Bull. Am. Phys. Soc. 26, 635 (1981).

[21] L. G. Arnold *et al.,* Phys. Rev. C 25, 936 (1982); L. G. Arnold, B. C. Clark, R. L. Mercer, and P. Schwandt, *ibid.* 23, 1949 (1981).

[22] F. A. Brieva and J. R. Rook, Nucl. Phys. A291, 299 (1977); A291, 317 (1977); A297, 206 (1978); A307, 493 (1978).

[23] H. V. von Geramb, F. A. Brieva, and J. R. Rook, in *Microscopic Optical Potentials,* edited by H. V. von Geramb, Lecture Notes in Physics Vol. 89 (Springer, Berlin, 1979), p. 104.

[24] F. D. Becchetti, Jr. and G. W. Greenlees, Phys. Rev. 182, 1190 (1969).

[25] J. P. Jeukenne, A. Lejeune, and C. Mahaux, Phys. Rev. C 16, 80 (1977).